11 Surface Physics

T. Greber, R. Holzner, E. Wetli, S. Dangel, T. J. Kreutz,
H. Schmid, P. Schwaller, H. Neff, J. Wider, W. Deichmann, J. Osterwalder

In our new surface physics laboratory (since 1995) we study fundamental physical and chemical processes on well-defined surfaces, using predominantly electron-based techniques such as photoelectron spectroscopy and electron diffraction. With these probes (X-ray photoelectron diffraction (XPD), medium-energy electron diffraction (MEED), low-energy electron diffraction (LEED)) we can determine atomic positions at surfaces with sub-Ångstrom precision. A time-resolved MEED experiment is being developed with a temporal resolution in the picosecond range. Angle-resolved UV photoelectron spectroscopy (ARUPS) gives us access to the electronic band structure of solids and surfaces. Here, we focus our attention onto the region near the Fermi energy ϵ_F where we could extend the measuring range of photoemission above the Fermi level to observe thermally excited electrons within the band structure. An important asset of these experiments is that the same probe (photoemission) gives us structural, electronic and magnetic information, and we can therefore study the interplay between these different degrees of freedom on the same sample.

Before presenting some of our first experimental results we should like to highlight the installation of a crucial piece of equipment in our photoelectron spectrometer. The monochromator for the VUV 5000 He discharge lamp was delivered by Gammadata Burklint AB, Sweden, by the end of July 1996. It focuses the light by means of a toroidal grating onto the sample. It was originally designed for gas phase experiments and was adopted in our laboratory for the angle scanned photoemission experiment from surfaces. The ECR plasma light source and the monochromator were tuned to a maximum photon flux with a minimum of gas load in the analysis chamber. The device is equipped now with a photon flux monitor. The monochromatized light intensity on the sample is $5 \cdot 10^{12}$ photons/s for HeIα (21.2 eV) and $2.4 \cdot 10^{12}$ photons/s for HeIIα on a spot with a diameter of 3 mm. In addition to the high intensity the source has a very high monochromaticity. For the He Iα radiation we can suppress higher energy He radiation from 11% in zero order diffraction by more than a factor of 50. It has to be emphasized that the high photon flux Φ yields with typical photoemission cross sections σ of 10Mb in this energy regime 'ionization times' $\tau = 1/\ \Phi\sigma$ in the order of one hour. This may give a limit for the observation time of surfaces that are sensitive to UV radiation.

11.1 Photoemission above the Fermi level

Together with the energy analyzer in the VG ESCALAB 220 spectrometer with an energy resolution of 20 meV and the fully automated 2π sample goniometer the system represents a unique photoemission experiment. In particular it is now possible to perform photoemission above the Fermi level. This is illustrated in Figure 11.1 where the photoemission intensity is shown in an energy window around the Fermi level of an Ag sample. In plotting the data on a semi-logarithmic scale (lower panel) it can be seen that

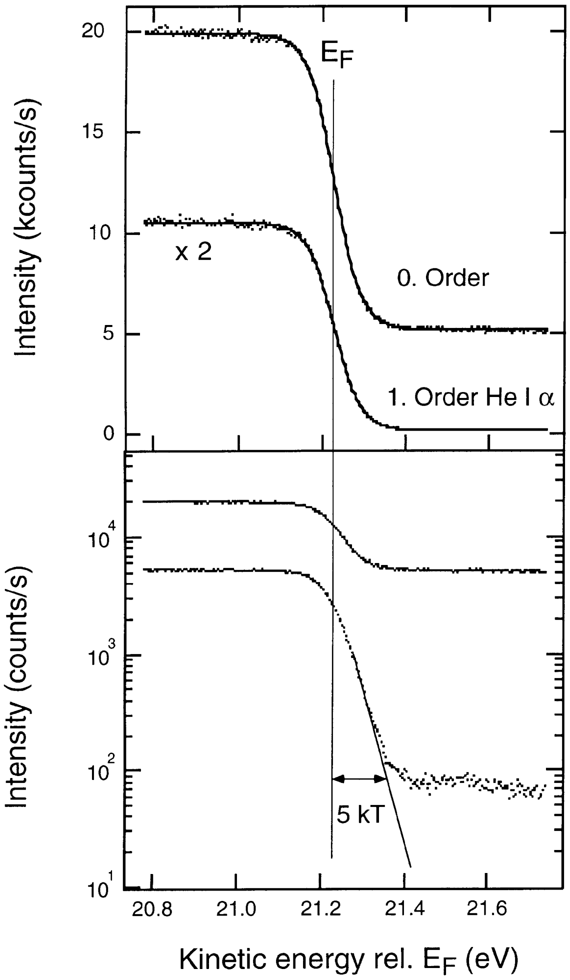

Figure 11.1: Photoemission spectra near the Fermi level of polycrystalline Ag, using unmonochromatized (zero order) and monochromatized (1st order) He I radiation. In the lower panel, a logarithmic intensity scale has been chosen for the same data.

with the monochromatized He Iα radiation the Boltzmann wing of the Fermi Dirac distribution can be measured up to 5kT above the Fermi level. For comparison the spectrum with non-monochromatized HeIα radiation is shown.

In order to demonstrate the feasibility band dispersion measurements above the Fermi level, i.e. the measurement of thermally excited electrons, the energy-momentum relation of the Ag(111) Shockley surface state [1] is plotted in Figure 11.2. The photoemission intensity rises from black in a linear gray scale. It is displayed as a function of binding energy and polar emission angle, which is related to the parallel component of the electron momentum. In a) the discontinuity in intensity at the Fermi level can be observed. The bright feature around θ=0° is assigned to transitions from the surface state. In b) the data along lines of constant energy

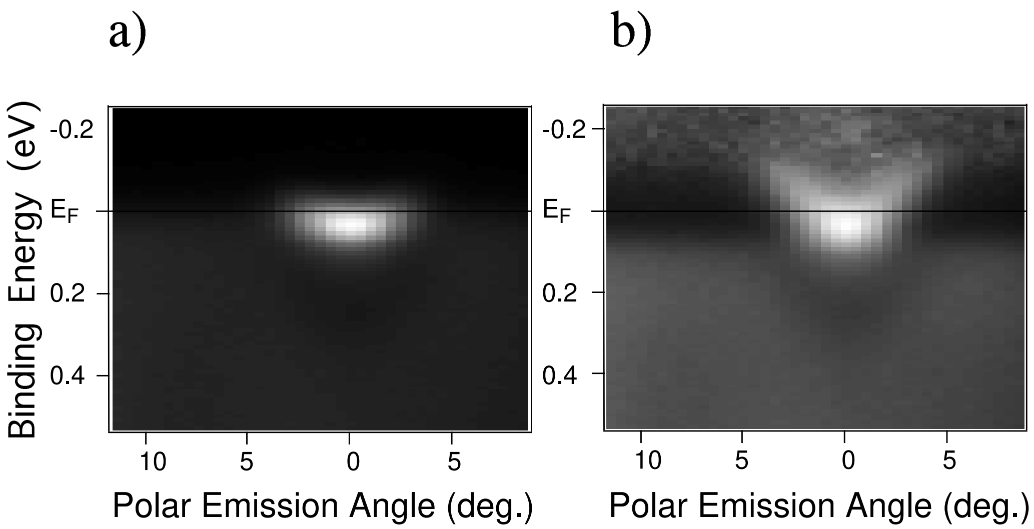

Figure 11.2: Polar intensity scan of photoemission spectra from Ag(111) near normal emission, using monochromatized He I radiation. Individual spectra (vertical lines) measured at a large number of angular settings have been combined to give this type of two-dimensional plot with photoemission intensities presented in a linear gray scale. The bright feature represents emission from the Shockley surface state near $\overline{\Gamma}$ of the surface Brillouin zone. In (a), the raw data are displayed, while (b) shows the data after a normalization procedure (see text).

have been normalized by the average intensity over all angles. As a consequence the parabolic dispersion of the surface state, indicating free electron-like behavior, can be observed even 100meV above the Fermi level. This new instrument for advanced photoemission therefore allows to map the unoccupied states within 5kT of ϵ_F up to the Brillouin zone boundary, i.e. to see unoccupied high-parallel-momentum electronic states. This should be particularly useful for observing the interplay between electrons and phonons at surfaces.

11.2 High-resolution photoemission from Ni(111)

In collaboration with P. Aebi and L. Schlapbach,
Institut de Physique, Universite de Fribourg

Nickel metal is a band ferromagnet. In the Stoner Model [2] [3], the electronic structure is described by two independent sets of energy bands for majority spin and minority spin electrons. The two sets are essentially equivalent, but shifted in energy by the amount $\Delta\epsilon_{ex}$, the exchange splitting. This simple model describes the ground state properties of Ni rather well, but the temperature-dependent phase transition to the paramagnetic state (T_c=631K) is not well reproduced. The calculated Curie temperature is nearly an order of magnitude too high. In the Stoner model the exchange splitting is directly related to the macroscopic magnetization, and it should thus vanish at T_c. On the other hand, neutron scattering data have clearly established the persistence of magnetic moments above T_c [4].

Angle-resolved photoemission is the most direct technique to investigate electronic bands in solids [5]. Previous interpretations of T-dependent photoemission data have been ambiguous: While the exchange splitting at low temperatures has been clearly observed, some experiments have claimed evidence for temperature-independent bands at specific directions in reciprocal space [6].

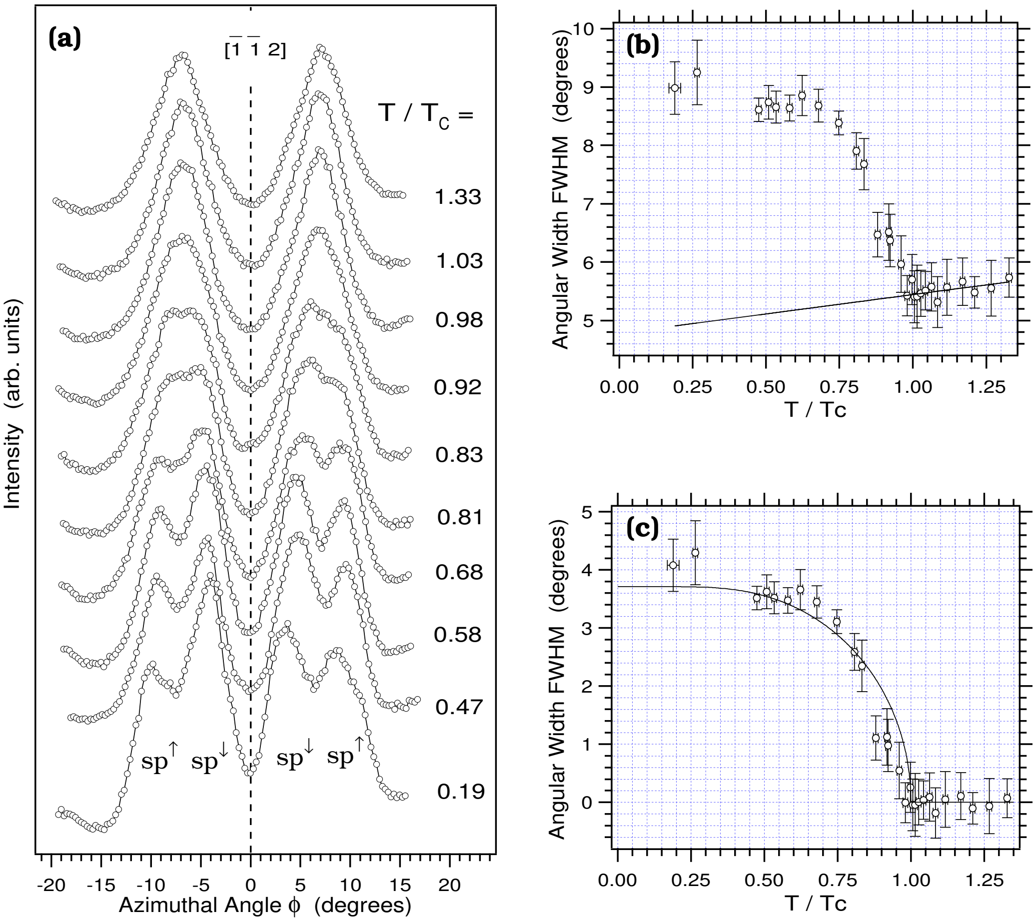

Figure 11.3: Temperature dependent exchange splitting of sp bands. In (a) azimuthal scans of Fermi-level intensities, taken at various temperatures from Ni(111) are presented. In (b) and (c), the full widths at half maximum intensity of exchange split peaks are shown before and after subtraction of a linear background, respectively. The solid line in (c) represents the temperature dependence of the macroscopic magnetization.

With our unique precision goniometer and high-resolution spectrometer we have revisited this issue [7]. As an example, Fig.11.3(a) shows azimuthal intensity variations of photoelectrons emitted from the Fermi level, measured for a series of temperatures. Peaks in these curves mark Fermi level crossings of various bands. In earlier publications we have identified these particular crossings with majority and minority sp bands, which are well separated in angle due to the exchange splitting [8]. Two pairs of spin-split $sp^{\uparrow}$ and $sp^{\downarrow}$ bands, related to each other by mirror symmetry across the $[\bar{1}\bar{1}2]$ azimuth, appear in the bottom curves. With rising temperature the pairs gradually coalesce, and for $T = 0.92T_c$ and higher we can distinguish only a single peak on each side. A simple measure for the change of the exchange splitting is the full width at half maximum of each pair. Fig. 11.3(b) shows the dependence of its value on temperature. The phase transition is clearly reflected in this curve, while phonon contributions produce a slowly rising background. Once this background is subtracted, the width, and thus the exchange splitting, follows the bulk magnetization curve rather closely. The sp electrons, which have a high group velocity, show here definitely a Stoner-like behaviour.

In Fig.11.4 we show photoemission data ($T = 0.47T_c$) from a different region in reciprocal space where we can watch the magnetic d-band crossing the Fermi level. In (a) we see the apex of the parabola of the fully occupied majority d-band, while the corresponding minority band parabola is intersected by the Fermi level where traditional photoemission experiments lose sight of it. Using the normalization procedure described in Section 11.1 we can fully recover the complete top of the minority band parabola (Fig. 11.4(b)). Figures (c) and (d) show the same reciprocal space region measured at $0.8T_c$, where the splitting has become considerably smaller, while (e) and (f) ($T = 1.21T_c$) are sets of spectra representing the paramagnetic state. Clearly the splitting has vanished, which suggests a Stoner-like behaviour also for these more localized states. However, the linewidth in energy is found to be anomalously large for $T > T_c$ which indicates deviations from this simple model.

11.3 High-resolution photoemission from Bi-cuprates

In collaboration with P. Aebi and L. Schlapbach, Institut de Physique, Universite de Fribourg, and H. Berger, Institut de Physique Appliquée, EPF Lausanne

Photoemission is an important player among the many experimental probes currently trying to unravel the mechanism of high-temperature superconductivity. We exploit the capability of our instrumentation to generate complete two-dimensional photoelectron patterns in order to map momentum distributions in reciprocal space. We performed such experiments previously at the University of Fribourg, where we measured e.g. the Fermi surface of optimally-doped $Bi_2Sr_2CaCu_2O_8$ [9]. While we were continuing these measurements in our new laboratory, using the high-flux UV source, we discovered an interesting photosensitivity which we did not expect in this type of oxides. Fig. 11.5a shows photoemission spectra of the region near the Fermi level from the same compound. One spectrum (thick line) was taken shortly after

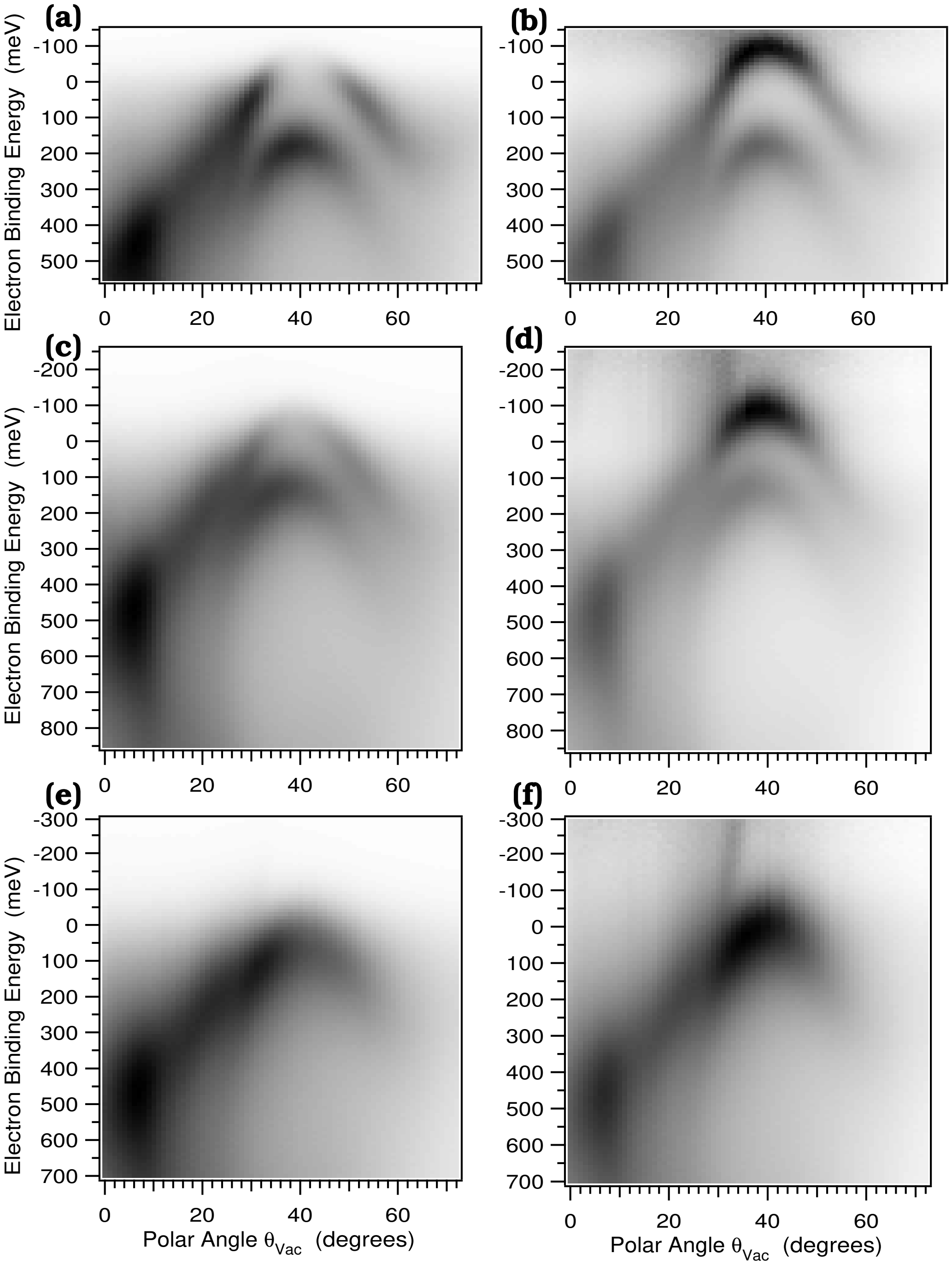

Figure 11.4: He I excited polar angle scans of energy spectra taken from Ni(111), measured at three different temperature. Raw data are presented on the left, the normalized data (see text) are given on the right. The linear gray scale ranges from minimum intensity (white) to maximum intensity (black). The sample temperatures were ($T = 0.47T_c$) in (a) and (b), $0.8T_c$ in (c) and (d), and ($T = 1.21T_c$) in (e) and (f).

cleaving the sample in UHV, while the second spectrum (thin line) represents the last of a long sequence of such spectra measured for this photosensitivity study. For each spectrum, a fitting procedure was done for a Fermi-Dirac distribution. Fig. 11.5b shows the resulting position of ϵ_F (dots) and the resulting width ("temper-

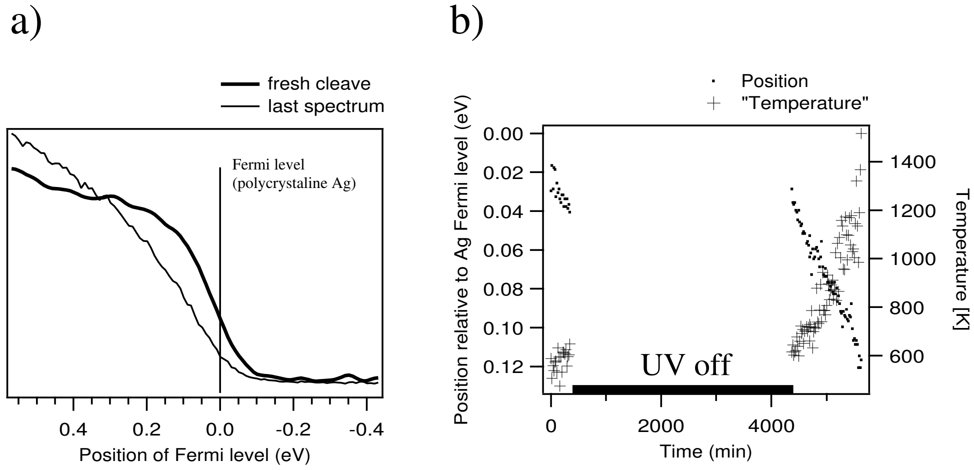

Figure 11.5: (a) Normal emission photoelectron spectra from $Bi_2Sr_2CaCu_2O_8$. The thick line shows the spectrum for a fresh cleave, the thin one the spectrum after approximately 30 hours under UV exposure. The reference Fermi level measured from a polycrystalline Ag sample is indicated by the vertical line. (b) Position and width ("Temperature") from a fit of the experimental spectra with a Fermi-Dirac distribution.

ature", crosses). Evidently the spectra show gradual changes with time, with the spectral weight receding away from the true Fermi level (as defined by the spectrometer) and the spectral distribution becoming broader. An important observation is that these changes take place only while the sample is exposed to UV light, while it is essentially stable when the lamp is switched off ("UV off").

We have not observed this photosensitivity in our earlier studies and attribute it to our high photon flux. At present investigate the mechanism behind this photoinduced sample aging. As a practical consequence from this experiment we have to reduce the photon flux onto these samples by a factor of about 10 in order to have stable measuring conditions for a fresh sample for a sufficient period of time.

11.4 Subsurface oxygen species on Rh(111)

In the traditional view of heterogeneous catalysis one pictures all molecular processes to take place on top of a more or less static catalytic surface. The only role of the catalyst is to chemisorb and dissociate the reacting molecules. There have, however, been indications that also the subsurface region of the catalyst may be involved in certain reactions. One system where a subsurface species of oxygen might play an important role as an oxygen reservoir is Rh(111) [10]. We have used XPD in order to observe the occupation of subsurface sites by oxygen atoms directly. In Fig. 11.6 a series of core-level photoemission spectra show the gradual oxygen uptake of this surface, reflected in the O 1s intensity, as a function of exposure (in Langmuir (L), i.e. $1.33 \cdot 10^{-6}$mbar sec.). After reaching a saturation near 5L, more oxygen is built into the surface for much higher exposures. In Fig 11.7 we see that the O 1s signal is more or less isotropic for $10^4 L$, which means that excess oxygen is bound in or on the surface layer, or it is highly disordered. The pattern observed for $10^5 L$ is a clear indication for the occupation of well-defined subsurface sites. An analysis by means of single-scattering cluster calculations suggests that octahedral sites between the first two rhodium layers are filled [11].

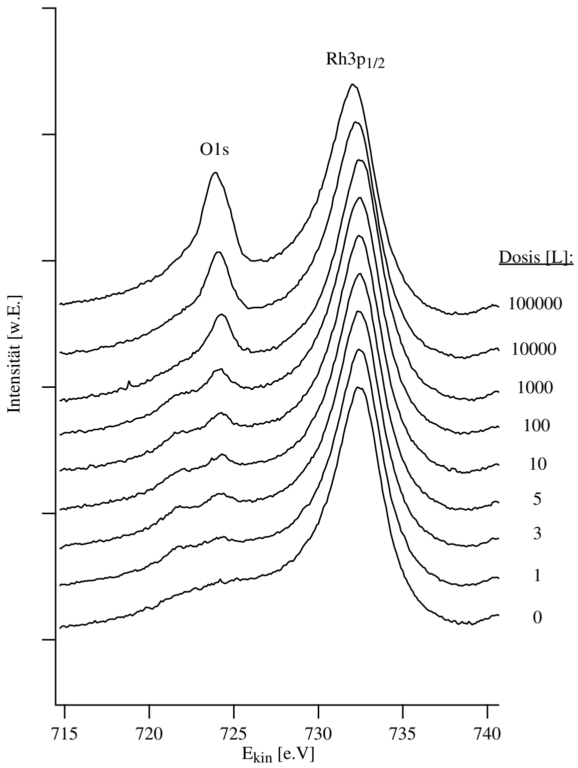

Figure 11.6: Mg Kα excited core level photoemission spectra from Rh(111) for various oxygen exposures. O 1s and Rh 3p$_1$/2 core levels are displayed.

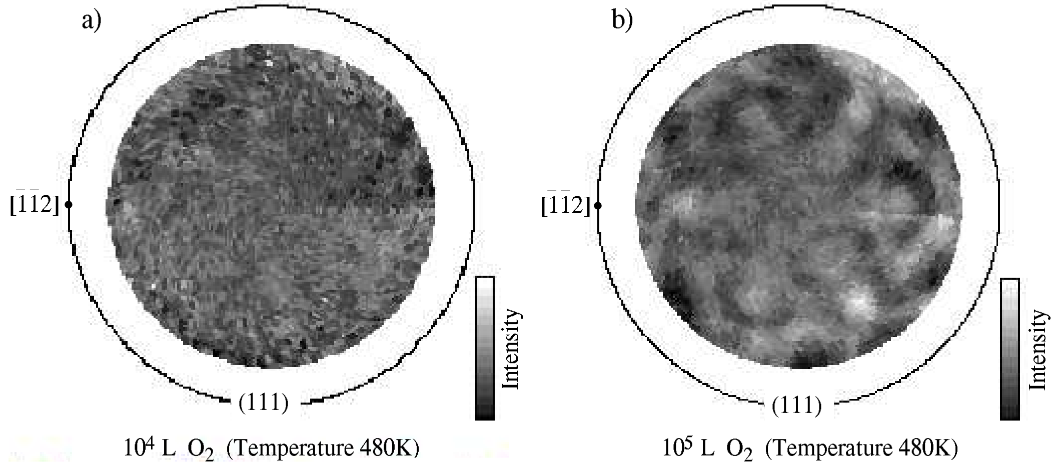

Figure 11.7: Mg Kα excited XPD patterns of O 1s emission from Rh(111) for oxygen exposures of 10^4L (a) and 10^5L (b). The plots present the angular distribution of O 1s intensities in a linear gray scale and in stereographic projection.

11.5 Time-resolved medium-energy electron diffraction

In collaboration with M. Aeschlimann, Institut für Technische Chemie, ETHZ.

As seen in the previous example XPD is a probe that provides direct information on local atomic sites in the surface region. MEED is a closely related technique. While it does not offer the chemical specificity of XPD it can be measured much faster. In a pump-probe experiment we try to extend the scope of this type of structural tool into the picosecond time regime. As such it would enable us to study the kinetics, and in favourable cases the dynamics of surface phase transitions and surface chemical reactions.

A pulsed electron gun has been constructed which, by using a 40 nm Ag photocathode and an ultrashort laser pulse, will produce electron pulses of less than 5 picoseconds at an energy of 2 keV. Using ray tracing methods, the electron optics has been optimized for minimum temporal dispersion for trajectories within a focus of 200 μm.

A new channelplate LEED detector has recently been purchased (OCI, London / Ontario, delivered in March 1997) and tested in the dedicated UHV chamber which is also fitted with the pulsed electron gun. The detector is capable of recording MEED patterns up to energies of 2000 eV, and due to its 4-grid electron optics it can be operated as a retarding-field analyzer for running Auger spectra for sample characterization. In Fig 11.8 (left) a first MEED pattern from W(001) is shown, measured at 1950 eV. The intensity pattern is very similar to the XPD pattern

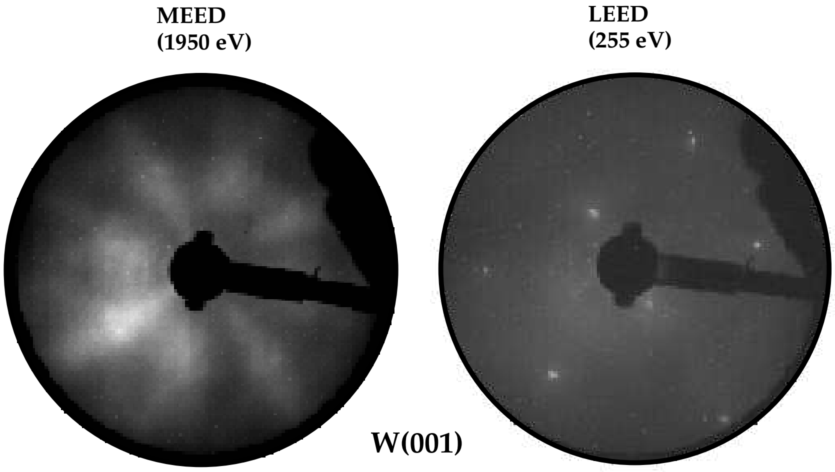

Figure 11.8: (left) MEED pattern from a W(001) single crystal surface, measured at an electron energy of 1950 eV. (right) LEED pattern at 255 eV, measured under identical conditions

measured for this same surface (not shown), because the scattering processes are in both cases dominated by strong forward scattering along crystal rows of atoms which render the intensity distribution characteristic of a body-centered cubic surface. In b) the LEED pattern, measured under the same conditions, indicates an excellent long-range crystal order of this surface. While these patterns were recorded with the electron beam at normal incidence to the surface, the pulsed beam can be set to grazing incidence. The MEED pattern should then reflect the geometry of the first two or three atomic layers.

11.6 Interaction of resonant laser light with sodium atoms close to a surface

When a surface is exposed to sodium vapor in a UHV chamber at room temperature, sodium atoms may be deposited on the surface either as single atoms, clusters or as a thin 2-dimensional film. Our aim is to demonstrate under these conditions laser-atom-interaction effects previously observed in a normal, three dimensional vapor [12]. One of these effects, called beamswitching [13], where one circularly polarized laser beam switches off another laser beam of opposite circular polarization may be of interest with regard to nanoscale all optical logical gates.

On our way to this goal we have compared the attachment of sodium at a plain glass surface and on a glass surface coated by a 25 Å thick self assembling monolayer (SAM) of organic molecules (octadecyltrichlorsilan OTS). Preliminary results using the absorption of a weak (1 mW/mm^2) 514 nm beam from an Ar-ion laser as a measure for the amount of sodium deposited on the surface show, that the attachment rate of sodium atoms is orders of magnitude smaller in the case of OTS coated glass compared to uncoated glass. Once sodium has been deposited it can also be desorbed by a somewhat stronger laser beam (500 mW/mm^2). A comparison (Fig.11.9) of the measured transmitted laser intensity through a thin sodium film on plain glass and results obtained from our thermal ablation model provide an estimate for the amount of deposited sodium, for heat conduction and black body radiation processes as well as the ablation dynamics [14].

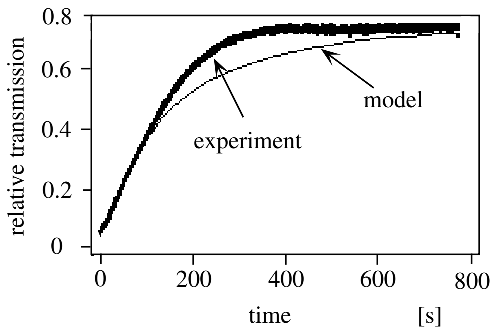

Figure 11.9: Comparison of laser induced desorption measurements with our thermal ablation model for a thin sodium film on plain glass

For the vapor deposition we use electric current operated sodium dispensers. An important information with regard to the sticking probability of sodium atoms at the surface, is the velocity and density distribution of sodium vapor leaving the dispenser exit slit. From Doppler shift measurements of the laser induced fluorescent radiation of the sodium atoms this information can be obtained. First measurements show that the average velocity of the atoms is about 500 m/s This corresponds to a temperature of about 140°C which is considerably less than the temperature of the red-hot dispenser. During these measurements we found an interesting geometrical relationship between the dispenser as a point-source for atoms and a light point-source formed by the scattering reflection of the laser beam on a glass plate (Fig.11.10). A simplified diagram of the situation is shown in Fig.11.11. Atoms leaving the dispenser with the same velocity but in different directions contribute to the fluorescent radiation if they are illuminated by the light point-source under the same angle α and for a given frequency (same Doppler shift). The fluorescent radiation of these atoms therefore originates from a sphere which contains the light source and the atom source. As a special case, if $\alpha = 90°$ (no Doppler shift) the light source and the atom source are the poles of the fluorescent sphere and all atoms independent of their velocity contribute to the fluorescent radiation. The light source is then tuned exactly to the atomic transition and the sphere appears bright and sharp. If the evolution of this sphere is recorded during a frequency scan of the laser, both density and velocity distribution of the atoms can in principle be determined.

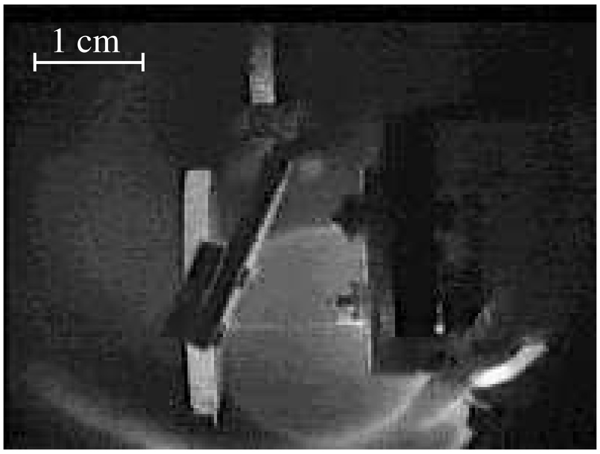

Figure 11.10: Sphere of laser induced fluorescent radiation from sodium atoms leaving an atom point-source and illuminated by a light point-source tuned exactly to the atomic D_1 transition.

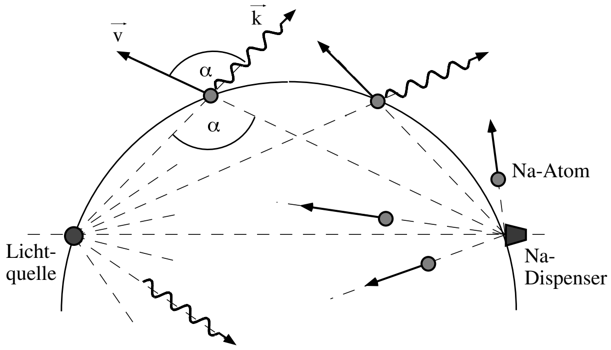

Figure 11.11: Geometrical relationship between the dispenser as a point-source for atoms and a light point-source formed by the scattering reflection of the laser beam on a glass plate creating a sphere of laser induced fluorescent radiation.

References

[1] H. F. Roloff, H. Neddermeyer, Solid State Commun. **21** (1977) 561.

[2] E.C. Stoner, Rept. Prog. Phys. **11** (1947) 43.

[3] E.P. Wohlfahrt, Rev. Mod. Phys. **25** (1953) 211.

[4] H.A. Mook, J.W. Lynn, R.M. Nicklow, Phys. Rev. Lett **30** (1973) 556.

[5] S.D. Kevan (ed.): Angle-Resolved Photoemission, Elsevier, Amsterdam (1992).

[6] K.-P. Kmper, W. Schmitt, G. Gntherodt, Phys. Rev. B **42** (1990) 10696.

[7] T. J. Kreutz, ph. d. thesis, University of Zürich (1997).

[8] T.J. Kreutz, P. Aebi, J. Osterwalder, Solid State Commun. **96** (1996) 339.

[9] P. Aebi, J. Osterwalder, P. Schwaller, L. Schlapbach, M. Shimoda, T. Mochiku, K. Kadowaki, Phys. Rev. Lett. **72** (1994) 2757.

[10] K. A. Peterlinz, S. J. Sibener, J. Phys. Chem. **99** (1995) 2817.

[11] J. Wider, diploma thesis, University of Zürich (1997).

[12] R. Holzner, J. Simonet, L. Flepp, B. Röhricht, P. Eschle, S. Dangel, U. Rusch, H. Schmid, and E. Brun, Optical Engineering **34** (1995) 2315–2323.

[13] S. Dangel, P. Eschle, B. Röhricht, U. Rusch, H. Schmid, and R. Holzner, J. Opt. Soc. Am. B, **12(4)** (1995) 681–686.

[14] H. J. Neff, diploma thesis, University of Zürich (1997).